The 0.5μm-2.22μm Scattered Light Spectrum of the Disk Around TW Hya[1]

John H.Debes[1], Hannah Jang-Condell[2],Alycia J. Weinberger[3], Aki Roberge[4], Glenn Schneider[5]

ABSTRACT

We present a 0.5-2.2μm scattered light spectrum of the circumstellar disk around TW Hya from a combination of spatially resolved HST STIS spectroscopy and NICMOS coronagraphic images of the disk. We investigate the morphology at the disk at distances $>$ 40 AU over this wide range of wavelengths. We measure the surface brightness, azimuthal symmetry, and spectral character of the disk as a function of radius. We find that the scattering efficiency of the dust is largely neutral to blue over the observed wavelengths. We find a good fit to the data over a wide range of distances from the star if we use a model disk with a partial gap of 30% depth at 80 AU and with steep disk truncation exterior to 100 AU. If the gap is caused by a planetary companion in the process of accreting disk gas, it must be less than 20 $M_{\oplus}$.

Subject headings: Stars:individual (TW Hya) — Protoplanetary Disks — Planet-disk interactions — Radiative transfer

---

[1]Space Telescope Science Institute, Baltimore, MD 21218

[2]University of Wyoming, Laramie, WY 82071

[3]Department of Terrestrial Magnetism, Carnegie Institution of Washington, Washington, D.C. 20015

[4]Goddard Space Flight Center, Greenbelt, MD 20771

[5]Steward Observatory, The University of Arizona, Tuscon, AZ 85721

[1]Based on observations made with the NASA/ESA Hubble Space Telescope, obtained at the Space Telescope Science Institute, which is operated by the Association of Universities for Research in Astronomy, Inc., under NASA contract NAS 5-26555. These observations are associated with program # 10167, 8624, 7226, and 7233.

1. Introduction

TW Hya is the closest example of a star with a young, gas-rich protoplanetary disk. As such, it is an ideal target in which to study how disk evolution is coupled to planet formation because the disk can be studied at high spatial resolution and with great sensitivity. First detected from its infrared excess (Rucinski & Krautter 1983), the disk emits strongly at wavelengths longer than 3 μm with a peak in its spectral energy distribution between 10 and 100 μm (Weinberger et al. 2002).

TW Hya may not be typical for its age. It is part of the eponymously named TW Hydrae Association, a collection of about two dozen stars, amongst which it sports the most massive, gas-rich disk of all. TW Hya is 54 $\pm$ 7 pc away in the new van Leeuwen (2007) Hipparcos catalog. The age of the TW Hya association is found from a variety of studies of the ensemble of stars, including measurements of the dynamics (8.3 $\pm$ 0.3 Myr) (Weinberger 2011; de la Reza et al. 2006), lithium depletion boundary (12 $\pm$ 8 Myr) (Mentuch et al. 2008), and these in combination with pre-main sequence tracks (10^{+10}_{-7} Myr) (Navascués 2006). Associations just a bit older than TW Hya, such as β Pic, have no optically thick, massive protoplanetary disks.

Despite reservations about its representativeness, intensive studies at every wavelength and spectral resolution have been used to try to understand the TW Hya disk's structure and composition. We summarize some of the main findings here. Resolved emission at 7mm indicated the central disk is mostly clear inside of 4 AU (Hughes et al. 2007). However, 2 μm emission resolved by the Keck Interferometer show that an optically thin dust disk comprised of small grains comes to within 0.06 AU of the star. The spectral energy distribution, particularly the large amount of emission at submm through cm wavelengths (Weintraub et al. 1989; Wilner et al. 2000; Weinberger et al. 2002; Wilner et al. 2005; Andrews et al. 2011) indicates substantial grain growth to at least cm sizes. Resolved CO line maps show the disk in Keplerian rotation with an inclination of 7 $\pm$ 1° beyond 50 AU (Qi et al. 2004; Andrews et al. 2011).

The disk has been spatially resolved in scattered light in the visible and near-infrared (Krist et al. 2000; Weinberger et al. 2002; Apai et al. 2004; Roberge et al. 2005). These show that the optically thick disk extends to at least 280 AU. They also show asymmetries and changes in surface brightness of the disk in the inner 150 AU. The presence of both small and large grains throughout the 4 AU - 200 AU disk and the presence of small grains in a region where they should quickly be removed, suggests that they are being regenerated through collisions at multiple locations.

The disk chemistry has also been probed in a spatially resolved manner in submm lines

(Qi et al. 2006). For example, there appears to be ongoing deuterium fractionation in the outer disk, and that suggests pristine nebular material is not preserved, as is often assumed for comets.

We have undertaken a multiwavelength visible to near-infrared study of scattered light from the disk in order to address several questions of interest to planet formation models. Observations in the visible to near-infrared can detect ices and silicates due to their broad absorption features and organics due to their red slopes. These types of observations are routinely applied to comets and Kuiper Belt objects, which are thought to be the planetesimal remnants of circumstellar disks. In addition, the spectral scattering efficiency of the disk can constrain the grain sizes at the disk surface. The mixture of grains should reflect a combination of vertical mixing from the midplane, where large grains are presumably formed, radial transport, and collisions. Finally but by no means least, we wish to understand the vertical structure of the disk and whether it shows evidence for forming planets.

2. Observations

We took coronagraphic images with the F171M, F180M, F204M, and F222M filters (central λ=1.71, 1.80, 2.04, and 2.22μm respectively) on 09 May 2005 with the NICMOS camera 2 for TW Hya and the PSF reference star, CD-43°2742 as part of Program GO 10167. The observations include direct images of both stars outside the coronagraphic hole with short exposures for point source photometry, as well as longer exposures for coronagraphic high contrast imaging. The instrumentally calibrated and reduced images discussed in this paper were created from the raw NICMOS *multiaccum* exposures following the processing methodolgy described by §3 of Schneider et al. (2005) and references therein.

For photometric analysis, each calibrated direct image was used to determine the total photometry of the star and empirically determine the scaling ratios between TW Hya and the PSF reference in each filter band. The three images for each star in each filter were located at different positions on the detector. We used a median combination of the three dither points to create a final image of each star to derive a ratio for scaling and for photometry of TW Hya. We used a 16.5 pixel radius circular aperture to determine the photometry. The background in the images is zero, so no background annulus was used. The individual dither points were used to get a rough estimate of the uncertainty in the ratios and photometry. Table 1 lists the photometry of TW Hya in each band with uncertainties and the scaling ratios for each filter.

In order to determine the best subtraction we minimized a chi-squared metric on a

region of the target image dominated by the star's diffraction spikes. We assumed that good subtraction of the diffraction spikes corresponded to the best subtraction of the PSF within the region of interest (Schneider et al. 2001). We iteratively created subtractions for combinations of scaling and pixel offsets until we found an image that produced the lowest chi-squared measure. We searched within 1-σ of the scaling ratios we determined above and within ± 1 pixel to find the best x and y pixel offsets.

To quantify the systematic effects on the photometry, we repeated the subtractions varying the PSF scalings and offsets by ± 1 σ from the minimum chi-square solution found above. Using a circular photometric aperture matched to the size of the disk, we found the standard deviation in the disk flux densities from this suite of subtractions. We then propagated this uncertainty into the total uncertainty in the flux density of the disk per pixel.

We observed TW Hya in each medium band filter at two distinct spacecraft orientations or roll angles. This is essentially an azimuthal dither that allows true objects within the field of view to be distinguished with instrumental artifacts that do not rotate with a change in orientation. The reference star, CD-43°2742, was subtracted from both roll-angle images to create two separate subtraction images for each filter. The images were then geometrically corrected for the slight optical distortion of the NICMOS camera 2 at the coronagraphic focus. We used the x-direction pixel scale of 0.″07595/pixel and the y-direction pixel scale of 0.″07542/pixel to create an image with pixels that have the y-direction plate scale in both directions. The geometrically corrected images were rotated to a common celestial orientation using the rotation centers given by the flight software in the raw data file headers. Figure 1 shows the resulting PSF subtracted images of the TW Hya disk taken in the medium band filters.

Additional observations of TW Hya with NICMOS were performed as a part of programs 7226 and 7223 with HST (Weinberger et al. 2002). The observations in F110W and F160W were recovered from the archive, reduced in the same manner as the medium band data, and median combined. Archival PSF reference stars for the images were subtracted from the target observations. The F110W reference was τ^1 Eridani, while the F160W reference was Gl 879. We followed the procedure of Weinberger et al. (2002) for scaling the PSFs, but followed the above procedure for subtraction.

TW Hya has been observed with STIS using a combination of wedge coronagraphic images as well as spatially resolved spectroscopy in the visible. The reduction for the data is detailed in Roberge et al. (2005). We used the same datasets that were presented in that work, with one exception. The spatially resolved STIS spectroscopy was re-extracted in 0.″35 distance bins to match our photometric apertures. Figures 1 and 2 shows the STIS and

NICMOS images of TW Hya.

3. Results

The observation of the disk in spatially resolved scattered light over a range of wavelengths allows a powerful look into both the morphology of the disk and the scattering efficiency of the disk's dust grains as a function of wavelength and distance from the star. In this Section we measure the surface brightness profiles, azimuthal asymmetries, and the scattering efficiency of the dust in the TW Hya disk.

3.1. Radial Surface Brightness Profiles in the Medium Band Filters

The radial structure of TW Hya belies its apparent smooth decrease in surface brightness as a function of radial distance. In fact TW Hya has some radial structure that deviates from what one would expect from a simple flared disk. We investigate the radial surface brightness profiles in our medium band NICMOS data and compare the behavior in these wavelengths to that seen in the shorter wavelength data.

Figure 3 shows the F171M through F222M surface brightness profiles. In all of them we see the characteristic shift in behavior between ~80-130 AU that is seen in the visible, 1.1, and 1.6μm, namely a change in the slope of the surface brightness. This feature is now seen in all the wavelengths of light in which TW Hya is observed, indicating that this is a feature caused by morphology rather than composition. We interpret this feature as a gap or depression in the disk, which we explore further in §4.2.

3.2. Azimuthal Surface Brightness Asymmetries

Roberge et al. (2005) measured the surface brightness as a function of azimuth for the 50CCD image of TW Hya's disk and found it possessed a significant asymmetry between 65-140 AU consistent with the asymmetry caused by a disk inclined to the line of sight with forward scattering dust grains. The magnitude and position of the asymmetry corresponded to a measured PA of the brightness maximum of 233.6°±4° and an inferred inclination of $15^{+8.7}_{-6.4}$° under the assumption of a Henyey-Greenstein scattering phase function for the grains with an asymmetry parameter g of 0.5. They found no significant asymmetry for larger radii.

In this paper we re-analyze the 50CCD images as well as the images at other passbands

to search for similar asymmetries For each passband, we took the final subtracted images and constructed photometric apetures in the shape of concentric annuli as a function of increasing radius with equal spacings of 0.″357 (20 AU). Each annulus was then further equally subdivided into azimuthal bins with width 20°. For each image a total of 6 annuli were used, from 0.″88 (50 AU) to 2.″31 (130 AU). For the 50CCD image, there was enough signal-to-noise to extend out to 3.″91 (220.7 AU). We therefore had a measure of the surface brightness distribution between 50-130 AU for all passbands, and a measure of the distribution for the 50CCD image and F110W image between 130 and 230 AU.

Certain areas of each image were masked out due to the presence of residual diffraction spikes or in the case of the 50CCD image, the presence of the occulting wedge. For apertures where masked pixels comprised more than 2/3 of the aperture, no surface brightness was calculated. Each annulus was then scaled to the median of the brightest annulus to provide equal weight to the surface brightness in any one azimuthal bin at each radius. The final azimuthal surface brightness distribution was then constructed by taking a median of the first six annuli for all images and another distribution was constructed for the 50CCD and F110W image of the disk from the final four annuli. For the uncertainty at each point we took the calculated photometric uncertainty or the standard deviation of the azimuthal points, whichever was larger.

Figure 4 shows the 50CCD and F110W results. Between 50 and 130 AU the asymmetry is similar in the two passbands. Beyond 130 AU, the character of the asymmetry is different: the minimum to maximum ratio of the asymmetry is smaller and the position of the maximum is not clearly aligned with that of the inner disk. The distance of 130 AU corresponds to a break in the radial suface brightness of the disk. For a comparison, we also overplot our best fitting scattered light models of the disk, described in more detail in §4.4, for inclinations of 7° and 15°.

Figure 5 shows the F160W, F171M, F180M, and F222M azimuthal brightness profiles. We neglect the F204M data because it has lower signal-to-noise. For each of these four images, no significant azimuthal asymmetry is revealed. Whatever is the cause of the asymmetry at shorter wavelengths, it is not detected with significance in the longer wavelength observations. We discuss the potential causes of this in §6.

3.3. Scattered Light Spectrum

The scattered light spectrum of the disk around TW Hya is a combination of the input stellar spectrum and the intrinsic spectrum of the disk. We removed the stellar spectrum of

TW Hya by dividing the measured surface brightness by the flux density of the star in each filter. We divided the STIS spectrum of the disk by the point source spectrum of the central star.

TW Hya is too bright to be directly imaged in the F110W and F160W filters as well as the unfiltered 50CCD observation. We therefore estimated the direct photometry of TW Hya in the unfiltered 50CCD observation, as well as the F110W and F160W filters using the CALCPHOT task of the SYNPHOT[1] package in conjunction with Kurucz models tabulated in the SYNPHOT library. We used a solar metallicity, $\log g$=4 model of a 3925 K star, assuming a luminosity of 0.25±0.06 $L_\odot$ based on a best fit match to TW Hya based on its estimated V magnitude during the STIS observation and parallax from the Hipparcos satellite and J, H, and K_s photometry from 2MASS. We compared the predicted F171M, F180M, F204M, and F222M photometry with the SYNPHOT values–they agreed to within a few percent of our measured photometry.

Figure 6 shows the total reflectance spectrum of the disk from 0.5-2.22μm and encompassing radial distances of between 50-230 AU. This data includes the average over the same distances of the STIS spatially resolved spectra of TW Hya from Roberge et al. (2005), normalized to the STIS photometric point. The overall spectrum is relatively neutral between 0.5-1.6μm, becoming more blue at longer wavelengths. No significant signature of sharp absorption lines are seen in any band. At longer wavelengths the disk becomes slightly bluer, possibly because of the presence of water ice in the observed dust.

4. Modeling the TW Hya Scattered Light Disk

In this Section we provide a model for the observed spectrum and morphology of the disk. This requires a model of the structure of the disk, discussed in §4.1. We infer that the depression we observe between 60-120 AU is caused by a "gap" in the disk. The origin of this feature will not be constrained by these observations, but a likely candidate is a planetary object that has succeeded in opening a gap. The limits to such a candidate are discussed in §5. However, other possibilities exist, which we outline in §6.

---

[1]http://www.stsci.edu/resources/software_hardware/stsdas

4.1. Initial Disk Structure

The disk models are generated as described in Jang-Condell (2008) and Jang-Condell & Turner (2011). The details of the radiative transfer modeling is also described in Jang-Condell & Sasselov (2003) and Jang-Condell & Sasselov (2004). The structure of the unperturbed planet-less disk is generated in a two-step procedure: (1) we calculate a locally plane-parallel two-dimensional model for the entire disk, then (2) we take a radially limited slice of this disk and refine its structure, this time taking the full three-dimensional (3D) curvature of the disk into account. In both steps, we iteratively calculate the vertical density and temperature structure of the disk including radiative transfer and under the assumption of hydrostatic equilibrium. The main heating sources are stellar irradiation and viscous heating.

In step (1), we use the same formalism developed by Calvet et al. (1991) and D'Alessio et al. (1998, 1999), with some simplifying assumptions. We calculate the disk from 0.25 to 256 AU, with radial bins spaced by factors of $\sqrt{2}$. At each radius, we assume that the disk is locally plane-parallel.

In step (2), we remove the assumption of local plane parallelness and calculate radiative transfer in three dimensions as a numerical integration over the surface of the disk. Although we assume that the overall disk structure is axisymmetric, the calculation of the radiative transfer is done in 3D to include the curvature of the disk both in vertical height above the midplane (z) and in the azimuthal direction (ϕ).

We adopt for our stellar and disk parameters those used by Calvet et al. (2002): effective temperature of $T_* = 4000$ K, radius $R_* = 1\,R_\odot$, and accretion rate of $5 \times 10^{-10}\,M_\odot \mathrm{yr}^{-1}$. This gives a total stellar luminosity of $L = 0.23 L_\odot$. One exception is stellar mass. Instead of 0.6 $M_\odot$, as chosen by Calvet et al. (2002), we choose a mass of 0.4 $M_\odot$ The mass of the central star TW Hya is not well known; it is inferred from the spectral type and pre-main sequence evolutionary tracks. The canonical literature spectral type is K7 (Webb et al. 1999) but recent infrared spectroscopy concludes the star is M2.5 and $T_{\rm eff}$=3400 K (Vacca & Sandell 2011). Most of the prior SED and sub-mm spectral cube modelling has assumed M_*=0.6 $M_\odot$ (Calvet et al. 2002; Qi et al. 2008), but the new spectral type implies a stellar mass of $0.4 M_\odot$. The main affect on our models of reducing the stellar mass is to make the disk puffier, hence able to intercept more stellar light, and therefore brighter, bringing it more into agreement with the measurements. We assume that the dust is well-mixed with the gas and constant throughout the disk, with a dust-to-gas ratio of 0.0138 and a grain-size distribution of $n(a) \propto a^{-3.5}$.

Calvet et al. (2002) found that large maximum grain sizes ($a_{\rm max}$) give good fits to the

SED of TW Hya at long wavelengths ($\lambda \gtrsim 1$ cm). Since there is a degeneracy between maximum grain size and viscosity parameter (α) in their models, they found that good fits to the SED of TW Hya are obtained with $a_{\rm max} = 1\,{\rm mm}, 1\,{\rm cm}$, or $10\,{\rm cm}$, with $\alpha = 5 \times 10^{-4}$, 3×10^{-4}, or 1×10^{-4}, respectively. This is because large grains are effectively invisible to optical and infrared wavelengths. The α parameter must be adjusted as the maximum grain size changes, because the overall mass of the disk increases with increasing grain size, assuming a fixed gas-to-dust ratio; however, the stellar mass accretion rate must be kept fixed. We find a similar degeneracy in our models, so we simplify our calculations by adopting $a_{\rm max} = 1\,{\rm cm}$ and $\alpha = 2.5 \times 10^{-4}$.

On the other hand, the scattered-light appearance of the disk is sensitive to the minimum grain size assumed, $a_{\rm min}$, and the composition of the grains. The wavelength dependent opacities are calculated using a Mie scattering code, miex, that includes distributions of particle sizes and can account for large dust particles (Wolf & Voshchinnikov 2004). For a model with a given minimum grain size, we recalculate the entire disk model from the initial conditions in order to be completely self-consistent.

4.2. Gap and Truncation

The gap in the disk is modeled as an ad hoc axisymmetric density perturbation parameterized by a Gaussian with adjustable width w and depth d centered at 80 AU. To model the truncation of the disk, we introduce an exponential cutoff at a knee k, as appears in the self-similar solution for an accretion disk as derived in Hartmann et al. (1998). If $\Sigma_0(r)$ is the unperturbed disk surface density, then the new surface density profile is

$$\Sigma(r) = \Sigma_0(r)\{1 - d\exp[-(r - 80\ {\rm AU})^2/(2w^2)]\}\exp[-(r/k)]. \quad (1)$$

Since the primary heating source for the disk is stellar irradiation, the effects of shadowing and illumination must be accounted for in determining the vertical structure of the disk. The three-dimensional density and temperature structure of the perturbed disk are calculated iteratively according to Jang-Condell (2008). That is, the illumination at the surface of the disk is determined by ray-tracing and the disk temperatures are calculated accordingly. Once the disk temperatures are determined, the vertical density profile of the disk is iteratively recalculated assuming hydrostatic equilibrium as above, keeping the vertically integrated surface density profile constant.

4.3. Scattered Light

The scattered light image of a disk is modeled as in Jang-Condell (2009) and Jang-Condell & Turner (2011). The scattering surface of the disk is defined to be where the optical depth from the star at a given frequency ν is $\tau_\nu = 2/3$. Then, the brightness at the scattering surface of the disk is

$$I_\nu^{\rm scatt} = \frac{\omega_\nu \mu R_*^2 B_\nu(T_*)}{4r^2(\mu + \cos i)} \tag{2}$$

where ω_ν is the albedo, μ is the cosine of the angle of incidence to the scattering surface, B_ν is the stellar brightness, r is the total distance to the star, and i is the angle between the line of sight to the observer and the normal to the scattering surface. The observed brightness of a star at distance d is

$$F_{\nu,\rm obs} = \pi B_\nu \left(\frac{R_*}{d}\right)^2 \tag{3}$$

so we can write express the surface brightness in scattered light in units of the apparent brightness of the star per square arcsecond:

$$I_\nu^{\rm scatt} = \frac{\omega_\nu \mu}{4\pi(\mu + \cos \iota)} \left(\frac{d}{\rm pc}\right)^2 \left(\frac{r^2 + z_s^2}{\rm AU^2}\right)^{-1} \left(\frac{F_{\nu,\rm obs}}{\rm asec^2}\right) \tag{4}$$

Finally, one needs to choose a composition and size distribution of the dust to calculate the final scattered light that is emitted from the disk. Many compositions and possible grain sizes are available, and it is not immediately clear whether a single composition is preferred for optically thick disks, or whether each individual disk has its own properties. The neutral color of TW Hya in the optical compared to the quite red colors of HD 100546, suggest that a range of compositions and size distributions exist amongst disks.

How predictive can models of optically thick disks be for composition and size distribution? In an attempt to answer this question, we have constructed six independent structure models that vary composition between pure water ice and astronomical silicates (Warren 1984; Laor & Draine 1993), and vary minimum grain sizes between 5×10^{-3},1, and 10μm. We take a fiducial disk model that has a maximum grain size of 1 cm, a gap width, w=30 AU, gap depth, d=0.3, located at a radius of 80 AU, and a truncation knee at k=100 AU. To calculate the expected scattering efficiency of the dust grains as a function of wavelength, we calculated albedo and opacity using the program miex (Wolf & Voshchinnikov 2004). The dust is well-mixed with the gas so that the dust density is proportional to the gas density.

Differing grain sizes and compositions can affect the resulting surface brightness profiles of a given disk structure. Figure 7 shows a comparison between the six predicted STIS surface

brightness profiles for the different models. If the composition of the disk is incorrect, the structure of the disk can be incorrectly interpreted.

In general, pure water ice disks are dimmer than those that possess pure silicates. The reason for this difference is primarily due to the higher opacity of a pure silicate disk, demonstrated in Figure 8. In this Figure we have plotted the height of the $\tau_\nu = 2/3$ surface (H) divided by the radius (R) for varying wavelengths. From Eq. (4), the brightness of the disk is proportional to the angle of incidence μ at the surface,

$$\mu \approx \frac{d}{dR}\left(\frac{H}{R}\right) - \frac{H}{R} = R\frac{d}{dR}\left(\frac{H}{R}\right) \tag{5}$$

If $H \propto R^\beta$, then $\mu = (\beta - 1)H/R$. Therefore, the brightness scales roughly with H/R. The H surface occurs higher up in the disk for silicates, resulting in a higher surface brightness. The different structure of the surface brightness profiles in Figure 7 is also striking, and is clarified by looking at $d(H/R)/dR$ for the different models (See Figure 9).

Water ice in particular has strong absorption features at 1.5 and 2.0 μm both wavelengths that are probed with our observations. Given the $\sim$10% accuracy of the disk photometry measurements, we can in principle detect absorption features in the medium band filters that have a depth of $\sim$15-30%. Figure 10 shows the resulting reflectance spectra for each of our models. Silicates show no sharp features in the visible to Near-IR, but are mostly neutral over this wavelength range for minimum grain sizes $>1\mu$m. Water ice shows noticeable features starting at $\sim 1\mu$m, but at the current levels of uncertainties in disk photometry, disks with minimum grain sizes of $>10\mu$m would be required to detect such a feature.

Based on our results above, composition can potentially play an important role in the observed scattered light spectrum as well as the observed surface brightness profiles of a disk. For our final model of TW Hya, an exhaustive search of compositions, grain sizes, and structures is computationally prohibitive and beyond the scope of this paper. We instead focused on dust opacities and scattering efficiencies using a composition with the same relative abundances as D'Alessio et al. (2001): 29.6% organics, 40.4% water ice, 24.5% astronomical silicates, and 5.5% troilite. This model composition successfully matches the SED of TW Hya. We can then determine whether such a composition is warranted for the surface of the disk based on the scattered light observations.

4.4. Model Parameters

We ran a suite of models, varying the following disk parameters as follows:

$$a_{\rm min} \in \{0.005, 0.5, 5\} \text{ microns} \tag{6}$$

$$w \in \{10, 20, 30\} \text{ AU} \quad (7)$$

$$d \in \{0.0, 0.3, 0.5\} \quad (8)$$

$$k \in \{60, 80, 100, 120, 150\} \text{ AU} \quad (9)$$

The surface brightness profiles are fit simultaneously spatially and across the 7 wavelengths for which we have photometric data. To account for uncertainties in the overall normalization such as might arise from uncertainty in the distance to TW Hya, we allow the overall brightness to vary by a constant factor and calculate the reduced χ^2 value for each model with respect to the data from 56 to 160 AU.

The best fit model is $a_{\min} = 0.005$ microns, $w = 10$ AU with a center at 80 AU, $d = 0.3$, and $k = 150$ AU. This has the lowest χ^2 as compared to the observed data of 2.45. The model brightness profile must be scaled by an overall factor of 1.07 to fit the data, meaning that the data is 7% brighter than our models and can be explained by the uncertainty in TW Hya's distance which could account for brightness differences of up to 23%.

Figures 11 and 12 show the radial data compared to the best fit model for all of the observations and radial spectral cuts of the disk. In general the model fits the observed spectrum quite well, with the exception of the region around 80 AU. This is also where the model fails to reproduce the observed surface brightness profile.

5. Mass of the Gap-Opening Planet

The best model for the TW Hya disk is one where an axisymmetric 30% partial gap is opened at 80 AU in the disk. A possible mechanism for opening such a gap is an embedded planet. The model we have used to fit to the TW Hya do not include hydrodynamics, but rather the gap is imposed in an ad hoc manner on the disk structure.

Numerical hydrodynamic simulations of planets embedded in gas-dominated protoplanetary disks by Bate et al. (2003) indicate that tidal torques between the planet and disk can clear axisymmetric partial gaps. In the case of an inviscid disk, the gap-opening threshold is roughly the mass at which the Hill radius of the planet equals the thermal scale height of the disk. The Hill radius of the planet is

$$r_{\text{Hill}} = \left(\frac{m_p}{3M_*}\right)^{1/3} a \quad (10)$$

where m_p is the mass of the planet, M_* is the mass of the star, and a is the star-planet

distance. The thermal scale height of the disk is

$$H = \frac{c_s}{v_\phi} a \tag{11}$$

where $c_s = \sqrt{kT/\mu}$ is the local thermal sound speed, k is the Boltzmann constant, T is the local disk temperature, μ is the mean molecular weight, $v_\phi = \sqrt{GM_*/a}$ is the orbital speed of the planet, and G is the gravitational constant. For a composition dominated by molecular hydrogen, $\mu = 2m_H$.

For a viscous protoplanetary disk, a more massive planet is required to open a similarly sized gap in a disk. The relation can be expressed as

$$\frac{3}{4}\frac{H}{r_{\rm Hill}} + \frac{50}{q\mathcal{R}} \lesssim 1 \tag{12}$$

(Crida et al. 2006), where $q = m_p/M_*$ and $\mathcal{R} \equiv r^2\Omega_P/\nu_v$ is the Reynolds number, and ν_v is the viscosity, given by $\nu_v = \alpha c_s H$ for an α-disk model.

Bate et al. (2003) adopt disk parameters of $H/r = 0.05$ and $\mathcal{R} = 10^5$ for their simulations, giving a gap-opening threshold of $q = 1.06 \times 10^{-3}$ using Eq. (12), or slightly more than 1 M_J. For comparison, the inviscid gap-opening threshold would be 0.4 M_J. They find that planets with $q = 3 \times 10^{-4}$ and 1×10^{-4} clear gaps of 90% and 50%, respectively, and a planet with $q = 3 \times 10^{-5}$ creates a nearly negligible gap. Thus, a planet that clears a gap of 30% would be between 0.03 and 0.1 of the viscous gap-opening threshold.

For TW Hya, our best-fit disk model has $H/r = 0.077$ and $\alpha = 2.5 \times 10^{-4}$, giving $\mathcal{R} = 7 \times 10^5$ and a viscous gap opening threshold of $q = 7.8 \times 10^{-4}$. Since $M_* = 0.4\,M_\odot$, this is 103 $M_\oplus$. This implies that if an embedded planet is the cause of the gap we have modeled, it must be between $3 - 10\,M_\oplus$. However, there is some degeneracy with regard to α, as discussed in §4.1. A larger value of α gives a lower Reynolds number, requiring a more massive planet to open a gap and allowing a larger planet to hide in the disk. If we adopt $\alpha = 5 \times 10^{-4}$, corresponding to a maximum grain size of 1 mm, we find a gap opening threshold of $q = 10^{-3}$. Thus, a more conservative upper limit on the mass of a planet at 80 AU in the TW Hya disk is 13 $M_\oplus$. If the mass of TW Hya is larger, these numbers will need to be revised upwards. However, a larger stellar mass also makes our disk models flatter and dimmer, which does not fit our scattered light images.

6. Discussion

We have combined several resolved images of the TW Hya disk in scattered light with spatially resolved spectroscopy of the disk. The spectrum of the disk in the visible and near-

IR is mostly featureless, with a broad neutral to blue trend, indicative of sub-micron grains. Based on our scattering models of the disk, a composition made primarily of organics, water ice, and silicates with grain sizes as small as $\sim$0.005μm best match the available scattered light data, and are consistent with models of TW Hya's SED.

We can compare our predicted water ice mass abundance relative to the models of Hogerheijde et al. (2011) based on their detection with Herschel of water vapor at 100-150 AU in the TW Hya disk. They interpreted the deficit of water vapor to that predicted by their models as evidence for dust settling of large icy grains to the disk midplane and assumed that there needed to be $> 9 \times 10^{27}$ g of water ice in the disk. Our scattered light images probe deeper in disk scale height than UV by definition and are more consistent with increasing water ice abundance, which would support the idea of dust grain settling. If we assume a disk mass in gas of $1.9{\times}10^{-2}$ $M_{\odot}$, assumed by Hogerheijde et al. (2011), then we would predict a total ice mass in the disk from our models of $2{\times}10^{2}9$ g, based on our mass abundance of 40% water ice in dust and a dust-to-gas ratio of 0.0138. Assuming that we probe the local mass abundance of water ice relative to gas at our $\tau = 2/3$ surface at the disk, this would imply a relative abundance of $5.6{\times}10^{-3}$ at 30 AU above the midplane at 100 AU and 46 AU above the midplane at 150 AU.

Our models, which include a 30% cleared gap at 80 AU and a disk truncation exterior to 150 AU match the observed surface brightness profiles as a function of wavelength. We have placed an upper limit on the mass of a planetary companion that could be clearing the gap seen in TW Hya to between $5 - 13\,M_{\oplus}$. Despite a general agreement between our models and the data, we discuss here some of the discrepancies and their potential causes.

The advantage of scattered light measurements is the ability to constrain minimum grain size since the smallest dust typically has the largest available surface area for scattering. Our models allow minimum grain sizes between 0.005 and 0.5 μm with nearly equivalent chi-sq values. By the absence of any strong water ice absorption features, we can constrain the abundance of water ice only on large grains; small grains show absorption features at <5% the disk scattering continuum even if wholly made of ice (see Figure 10), below the level of our disk photometric uncertainties. We have chosen a composition based on what is most likely present in the TW Hya disk, but we have not exhaustively explored other materials. Any material that scatters neutrally in the visible to near-IR would most likely also be suitable to explain the spectral shape we observe. To test multiple grain sizes requires a self-consistent model with different parameters used by D'Alessio et al. (2001). Our current models for TW Hya are being expanded to include these effects to better model the disk (Jang-Condell 2011, in prep).

Besides color, the other main effect of grain size is on the overall surface brightness of the

disk, and the higher albedo of smaller grains helps match the data. Yet, our models slightly underpredict the measured brightness; we need to scale the model by a factor of $\sim$1.07. The presence of higher opacity grains of neutral color, possibly the presence of more silicates in the small grains, could make the disk brighter yet. This may argue for fewer organics and ices in the TW Hya disk. Dust of size comparable to the wavelength is expected to forward-scatter; however, including forward scattering would decrease the overall brightness of the disk because we observe mainly 90° scattering.

Interestingly, the brightness asymmetry between the front and back sides of the disks is only apparent at wavelengths $\leq$1.1μm, and the brightness asymmetry for wavelengths longer than 1.1μm are not well fit by our models if we assume some disk inclination. The short wavelengths probe the uppermost disk surface where the bulk of the vertical height of the disk is optically thick to them. This suggests that the brightness asymmetry is caused by a perturbation in the surface grains only.

While our models are of the outer disk, which is mainly illuminated by the central star and not affected by accretion, the general framework of the α viscosity disk does set the disk viscosity and therefore the ease with which a gap is opened. The upper limit of the gap-opening mass depends approximately linearly on the viscosity, which in turn is derived from the measured accretion rate.

Finally, we investigate other possibilities for the presence of the gap. It is interesting to note in Figure 12 that at 80 AU, the center of the gap, the spectral character of the disk is different than that seen in other portions of the disk. If this is real, then a different composition in this annulus may be causing the overall structure of the disk to change. Conversely, compositional changes in this gap might be caused by enhanced collisions within the disk or the presence of an accreting protoplanet. Both of these possibilities are supported in part by the recent discovery to a sharp cutoff in the millimeter emission from dust at 60 AU, which is not present in similar high resolution imaging of CO gas (Andrews et al. 2011). Since we see scattered light from dust well beyond this cut-off it is clearly due to a change in the bulk size distribution or millimeter emission properties of the dust, which in of itself may be a signature of a planetary companion or change in bulk dust composition.

The gap could instead be an unresolved spiral structure in the disk, as seen in HD 141569 (Clampin et al. 2003). This could explain both the asymmetry as well as the decrease in surface brightness. Higher spatial resolution images, such as from next generation ground based AO coronagraphs, might solve the mystery. But the rather small field of view for these instruments ($\sim$2$''$=112 AU) might not be able to probe these interesting features in the TW Hya disk effectively.

Support for program #10167 was provided by NASA through a grant from the Space Telescope Science Institute, which is operated by the Association of Universities for Research in Astronomy, Inc., under NASA contract NAS 5-26555.

REFERENCES

Andrews, S. M., Wilner, D. J., Hughes, A. M., Qi, C., Rosenfeld, K. A., Oberg, K. I., Birnstiel, T., Espaillat, C., Cieza, L. A., Williams, J. P., Lin, S.-Y., & Ho, P. T. P. 2011, ArXiv e-prints

Apai, D., Pascucci, I., Brandner, W., Henning, T., Lenzen, R., Potter, D. E., Lagrange, A.-M., & Rousset, G. 2004, A&A, 415, 671

Bate, M. R., Lubow, S. H., Ogilvie, G. I., & Miller, K. A. 2003, MNRAS, 341, 213

Calvet, N., D'Alessio, P., Hartmann, L., Wilner, D., Walsh, A., & Sitko, M. 2002, The Astrophysical Journal, 568, 1008, (c) 2002: The American Astronomical Society

Calvet, N., Patino, A., Magris, G. C., & D'Alessio, P. 1991, ApJ, 380, 617

Clampin, M., Krist, J. E., Ardila, D. R., Golimowski, D. A., Hartig, G. F., Ford, H. C., Illingworth, G. D., Bartko, F., Benítez, N., Blakeslee, J. P., Bouwens, R. J., Broadhurst, T. J., Brown, R. A., Burrows, C. J., Cheng, E. S., Cross, N. J. G., Feldman, P. D., Franx, M., Gronwall, C., Infante, L., Kimble, R. A., Lesser, M. P., Martel, A. R., Menanteau, F., Meurer, G. R., Miley, G. K., Postman, M., Rosati, P., Sirianni, M., Sparks, W. B., Tran, H. D., Tsvetanov, Z. I., White, R. L., & Zheng, W. 2003, AJ, 126, 385

Crida, A., Morbidelli, A., & Masset, F. 2006, Icarus, 181, 587

D'Alessio, P., Calvet, N., & Hartmann, L. 2001, ApJ, 553, 321

D'Alessio, P., Calvet, N., Hartmann, L., Lizano, S., & Cantó, J. 1999, ApJ, 527, 893

D'Alessio, P., Canto, J., Calvet, N., & Lizano, S. 1998, ApJ, 500, 411

de la Reza, R., Jilinski, E., & Ortega, V. G. 2006, The Astronomical Journal, 131, 2609, (c) 2006: The American Astronomical Society

Hartmann, L., Calvet, N., Gullbring, E., & D'Alessio, P. 1998, ApJ, 495, 385

Hogerheijde, M. R., Bergin, E. A., Brinch, C., Cleeves, L. I., Fogel, J. K. J., Blake, G. A., Dominik, C., Lis, D. C., Melnick, G., Neufeld, D., Panić, O., Pearson, J. C., Kristensen, L., Yıldız, U. A., & van Dishoeck, E. F. 2011, Science, 334, 338

Hughes, A. M., Wilner, D. J., Calvet, N., D'Alessio, P., Claussen, M. J., & Hogerheijde, M. R. 2007, The Astrophysical Journal, 664, 536, (c) 2007: The American Astronomical Society

Jang-Condell, H. 2008, ApJ, 679, 797

—. 2009, ApJ, 700, 820

Jang-Condell, H. & Sasselov, D. D. 2003, ApJ, 593, 1116

—. 2004, ApJ, 608, 497

Jang-Condell, H. & Turner, N. 2011, submitted

Krist, J. E., Stapelfeldt, K. R., Ménard, F., Padgett, D. L., & Burrows, C. J. 2000, The Astrophysical Journal, 538, 793, (c) 2000: The American Astronomical Society

Laor, A. & Draine, B. T. 1993, ApJ, 402, 441

Mentuch, E., Brandeker, A., van Kerkwijk, M. H., Jayawardhana, R., & Hauschildt, P. H. 2008, The Astrophysical Journal, 689, 1127, (c) 2008: The American Astronomical Society

Navascués, D. B. Y. 2006, Astronomy and Astrophysics, 459, 511

Qi, C., Ho, P. T. P., Wilner, D. J., Takakuwa, S., Hirano, N., Ohashi, N., Bourke, T. L., Zhang, Q., Blake, G. A., Hogerheijde, M., Saito, M., Choi, M., & Yang, J. 2004, ApJ, 616, L11

Qi, C., Wilner, D. J., Aikawa, Y., Blake, G. A., & Hogerheijde, M. R. 2008, ApJ, 681, 1396

Qi, C., Wilner, D. J., Calvet, N., Bourke, T. L., Blake, G. A., Hogerheijde, M. R., Ho, P. T. P., & Bergin, E. 2006, The Astrophysical Journal, 636, L157, (c) 2006: The American Astronomical Society

Roberge, A., Weinberger, A. J., & Malumuth, E. M. 2005, The Astrophysical Journal, 622, 1171, (c) 2005: The American Astronomical Society

Rucinski, S. M. & Krautter, J. 1983, Astronomy and Astrophysics (ISSN 0004-6361), 121, 217

Schneider, G., Becklin, E. E., Smith, B. A., Weinberger, A. J., Silverstone, M., & Hines, D. C. 2001, AJ, 121, 525

Schneider, G., Silverstone, M. D., & Hines, D. C. 2005, ApJ, 629, L117

Vacca, W. D. & Sandell, G. 2011, ApJ, 732, 8

van Leeuwen, F. 2007, Springer

Warren, S. G. 1984, Appl. Opt., 23, 1206

Webb, R. A., Zuckerman, B., Platais, I., Patience, J., White, R. J., Schwartz, M. J., & McCarthy, C. 1999, ApJ, 512, L63

Weinberger, A. J. 2011, in prep

Weinberger, A. J., Becklin, E. E., Schneider, G., Chiang, E. I., Lowrance, P. J., Silverstone, M. D., Zuckerman, B., Hines, D. C., & Smith, B. A. 2002, The Astrophysical Journal, 566, 409, (c) 2002: The American Astronomical Society

Weintraub, D. A., Sandell, G., & Duncan, W. D. 1989, ApJ, 340, L69

Wilner, D. J., D'Alessio, P., Calvet, N., Claussen, M. J., & Hartmann, L. 2005, The Astrophysical Journal, 626, L109, (c) 2005: The American Astronomical Society

Wilner, D. J., Ho, P. T. P., Kastner, J. H., & Rodríguez, L. F. 2000, The Astrophysical Journal, 534, L101, (c) 2000: The American Astronomical Society

Wolf, S. & Voshchinnikov, N. V. 2004, Computer Physics Communications, 162, 113

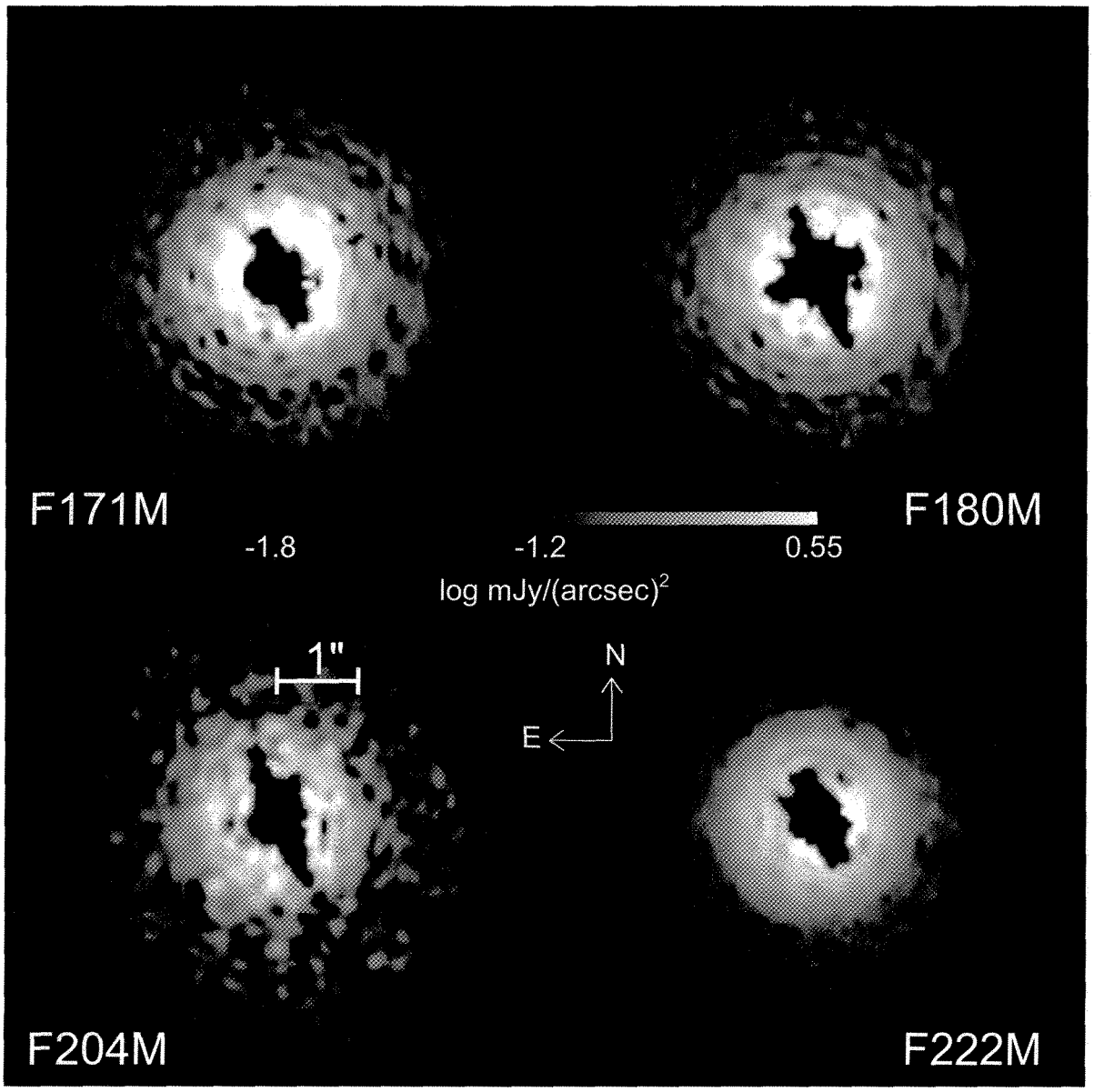

Fig. 1.— Final, roll combined, PSF-subtracted images of TW Hya in the four medium band filters observed, F171M, F180M, F204M, and F222M.Regions in which there is no data, i.e. under the coronagraph plus in an extended region in the NE/SW diffraction spike are blacked out. The mottled appearance in the shorter filters, particularly F204M, is the result of systematic residuals from diffraction and scattering patterns. The bright diagonal stripe at lower SW is from the edge of the NIC-2 array.

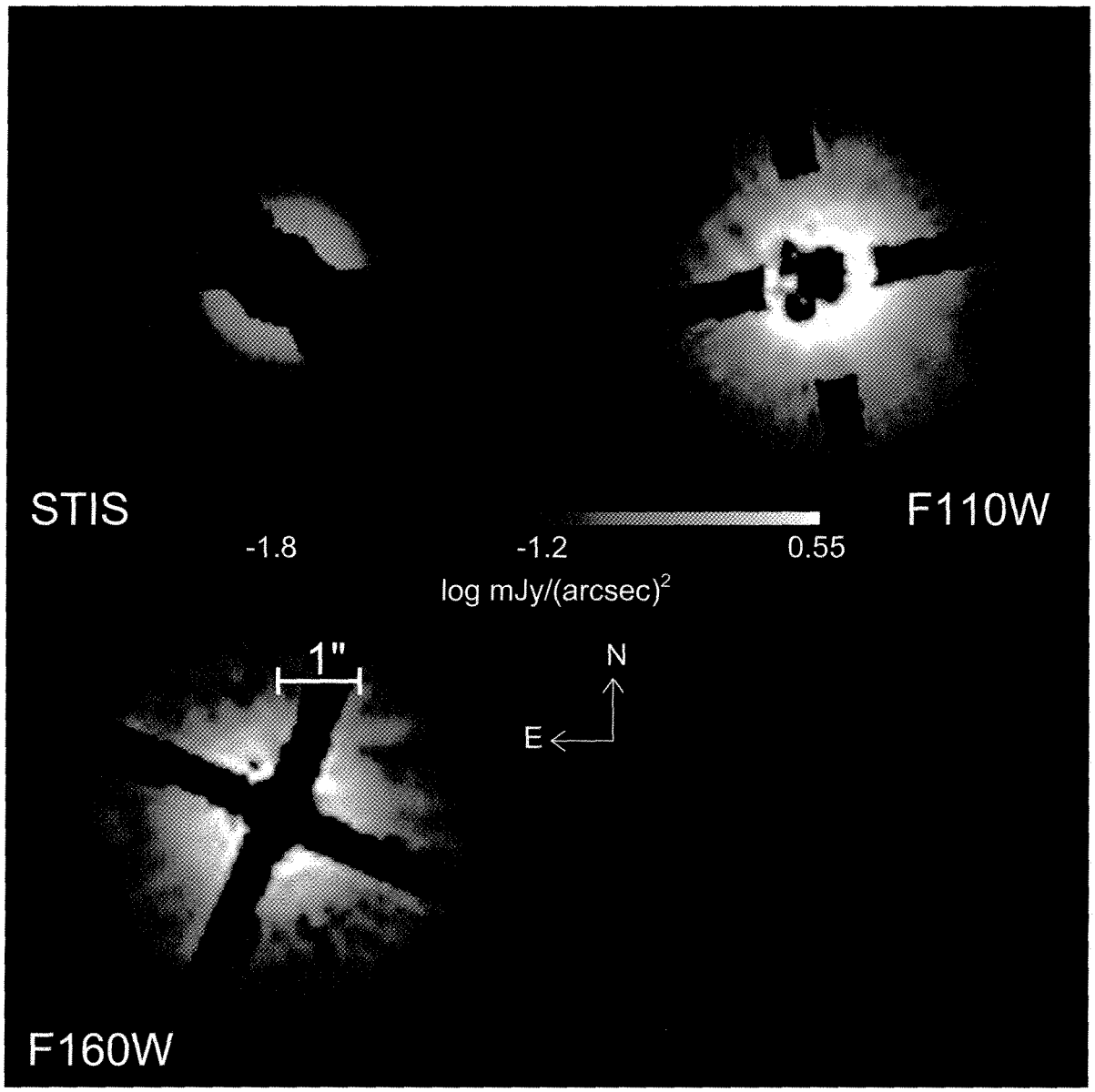

Fig. 2.— Final images from previous scattered light observations of TW Hya with STIS, NICMOS' F110W filter, and F160W filter.

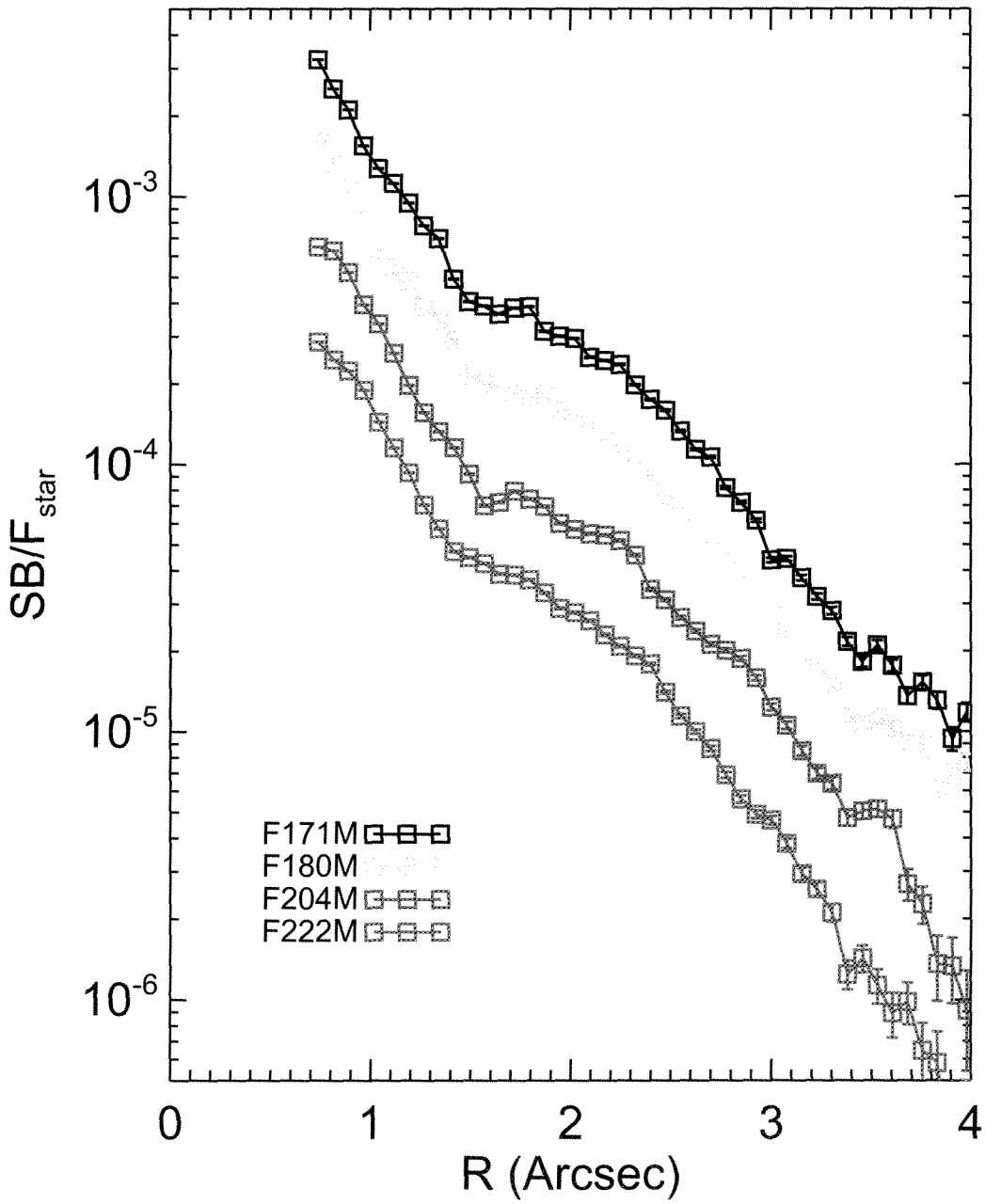

Fig. 3.— Surface brightness profiles of the TW Hya disk at 1.71, 1.80, 2.04, and 2.22 μm. The 1.80, 2.04, and 2.22 μm curves are scaled by factors of 0.5, 0.25, and 0.125 respectively.

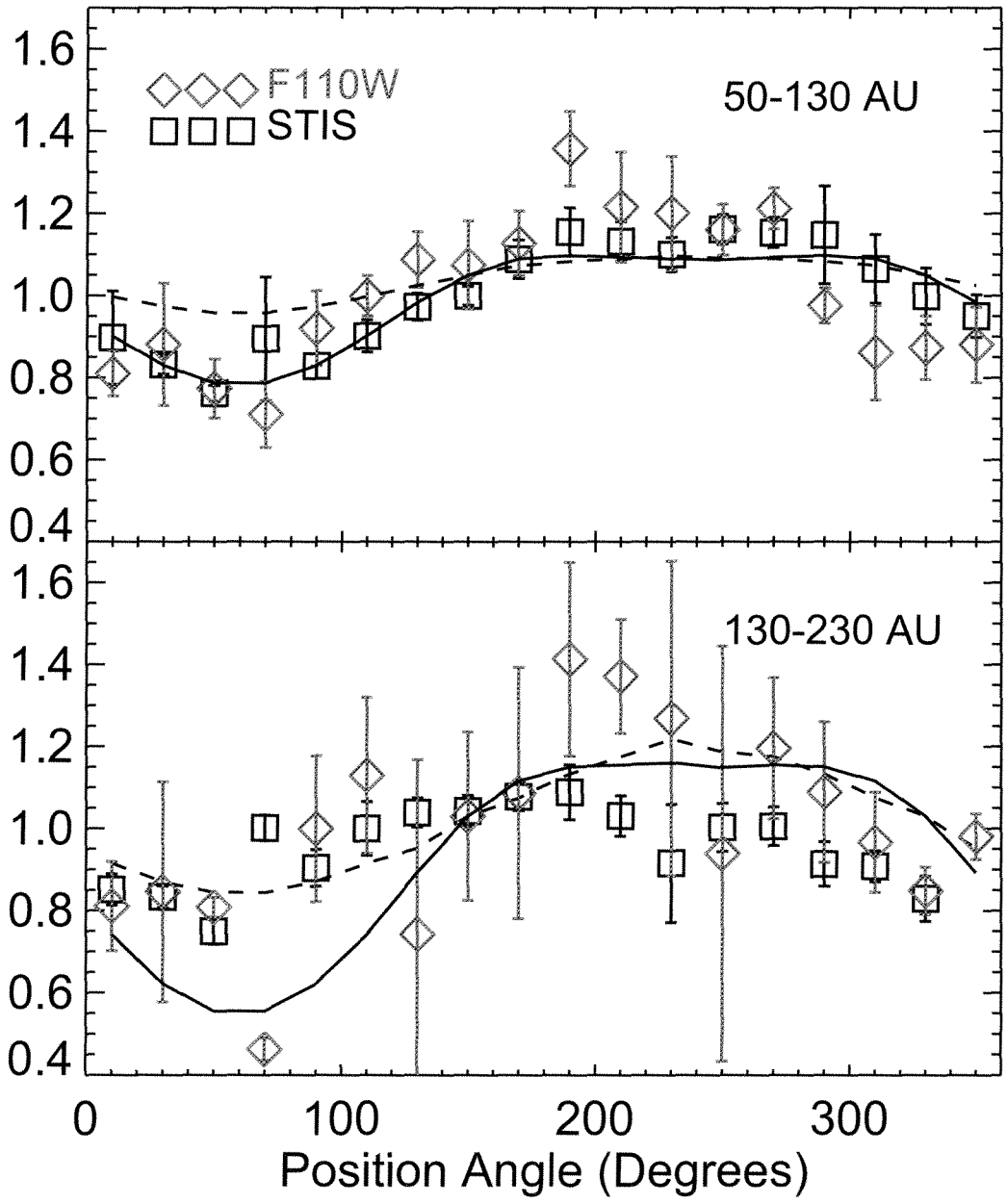

Fig. 4.— Azimuthal brightness profiles for the STIS and F110W images between 50-130 AU (top) and 130-230 AU (bottom). Each curve was normalized by the median surface brightness. In each panel we compare the brightness asymmetry with that of our best fitting model disk in §4.4 with inclinations of 15° (solid line) and 7° (dashed line).

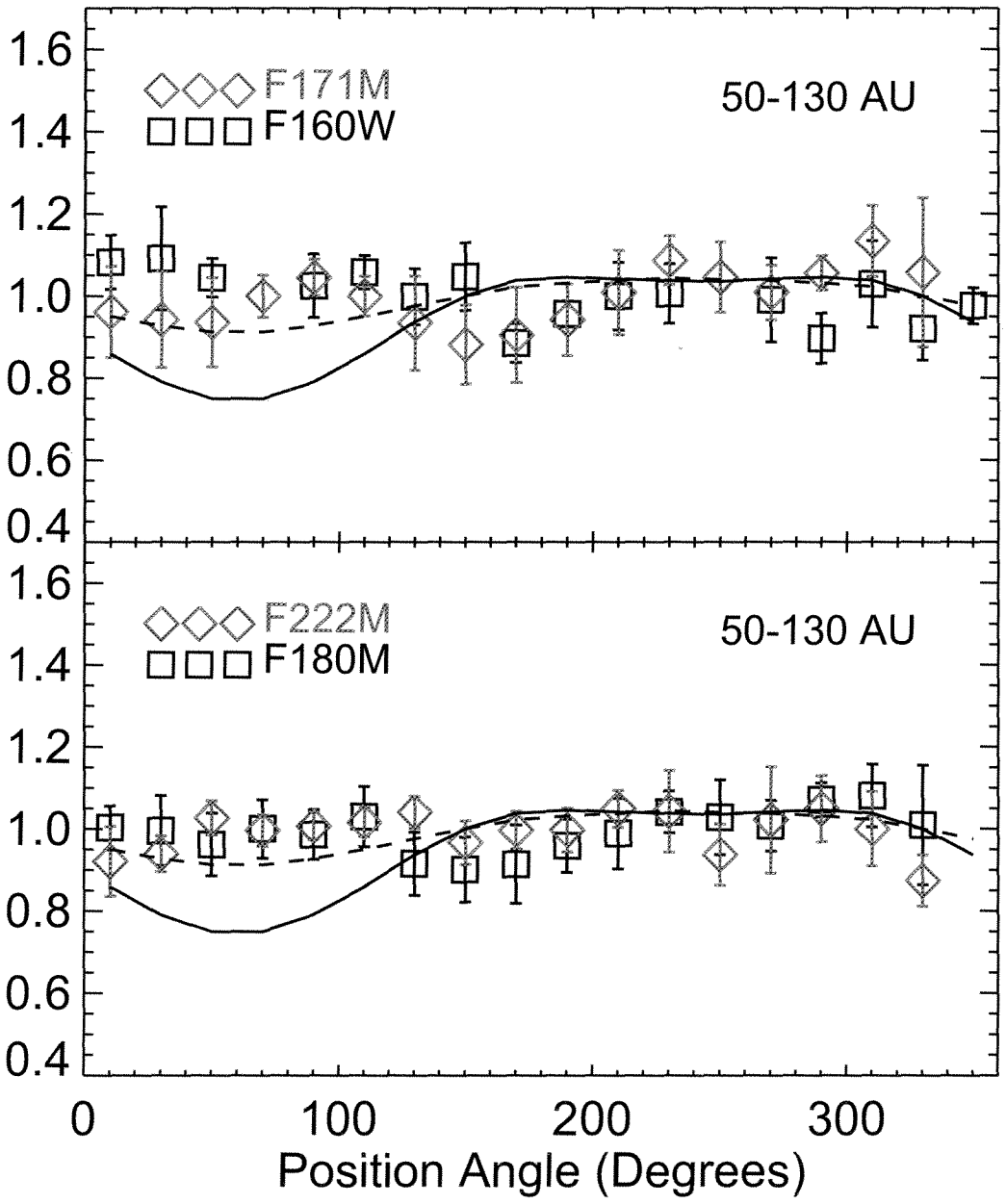

Fig. 5.— Azimuthal brightness profiles for the F160W and F171M images between 50-130 AU (top) and the F180M and F222M images between 50-130 AU (bottom). Each curve was normalized by the median surface brightness. In each panel we compare the brightness asymmetry with that of our best fitting model disk in §4.4 with inclinations of 15° (solid line) and 7° (dashed line).

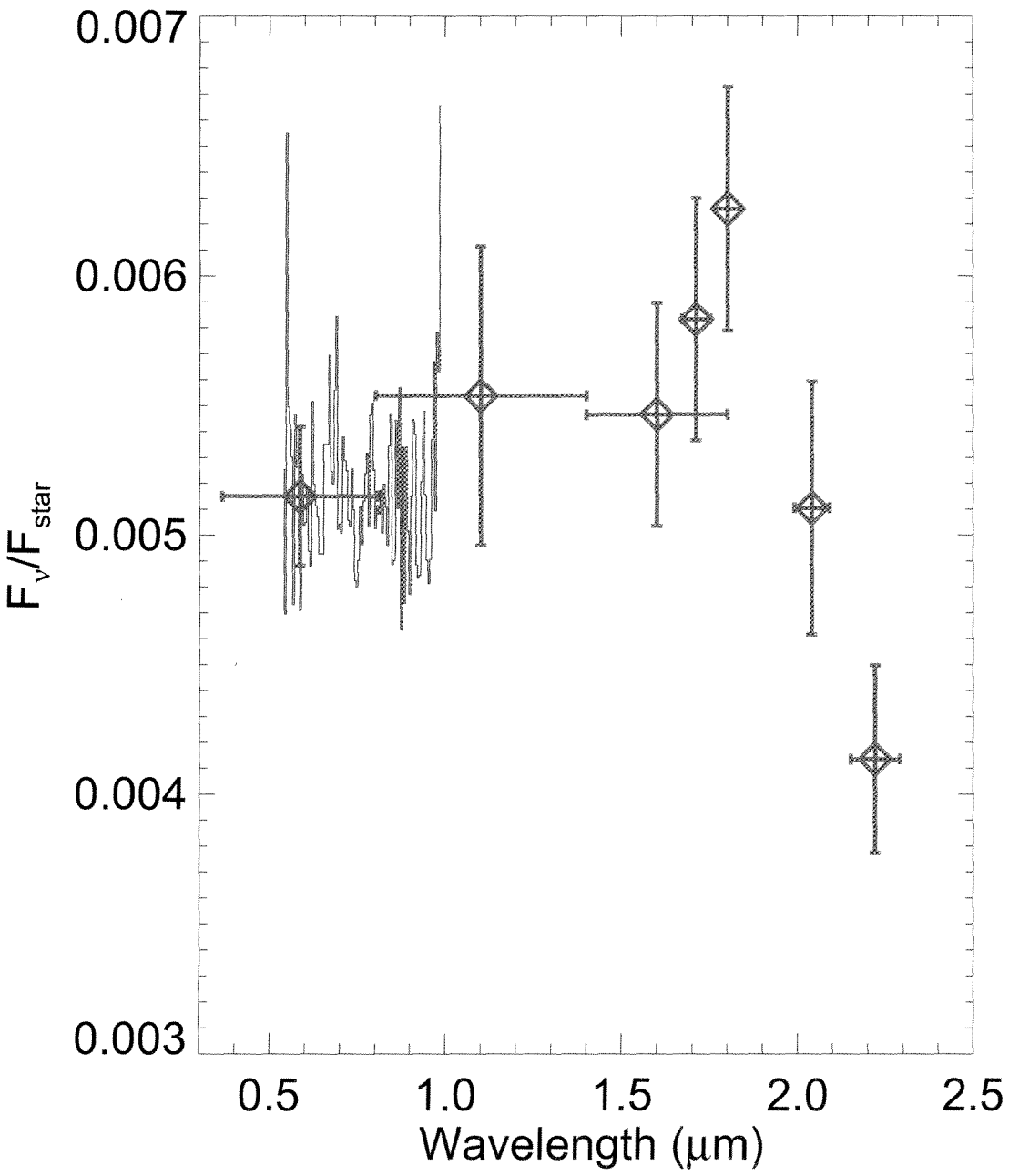

Fig. 6.— Total spectral reflectance of the TW Hya disk from 0.5-2.22μm, including an average of the spatially resolved spectra of TW Hya from Roberge et al. (2005) normalized to the STIS disk photometry.

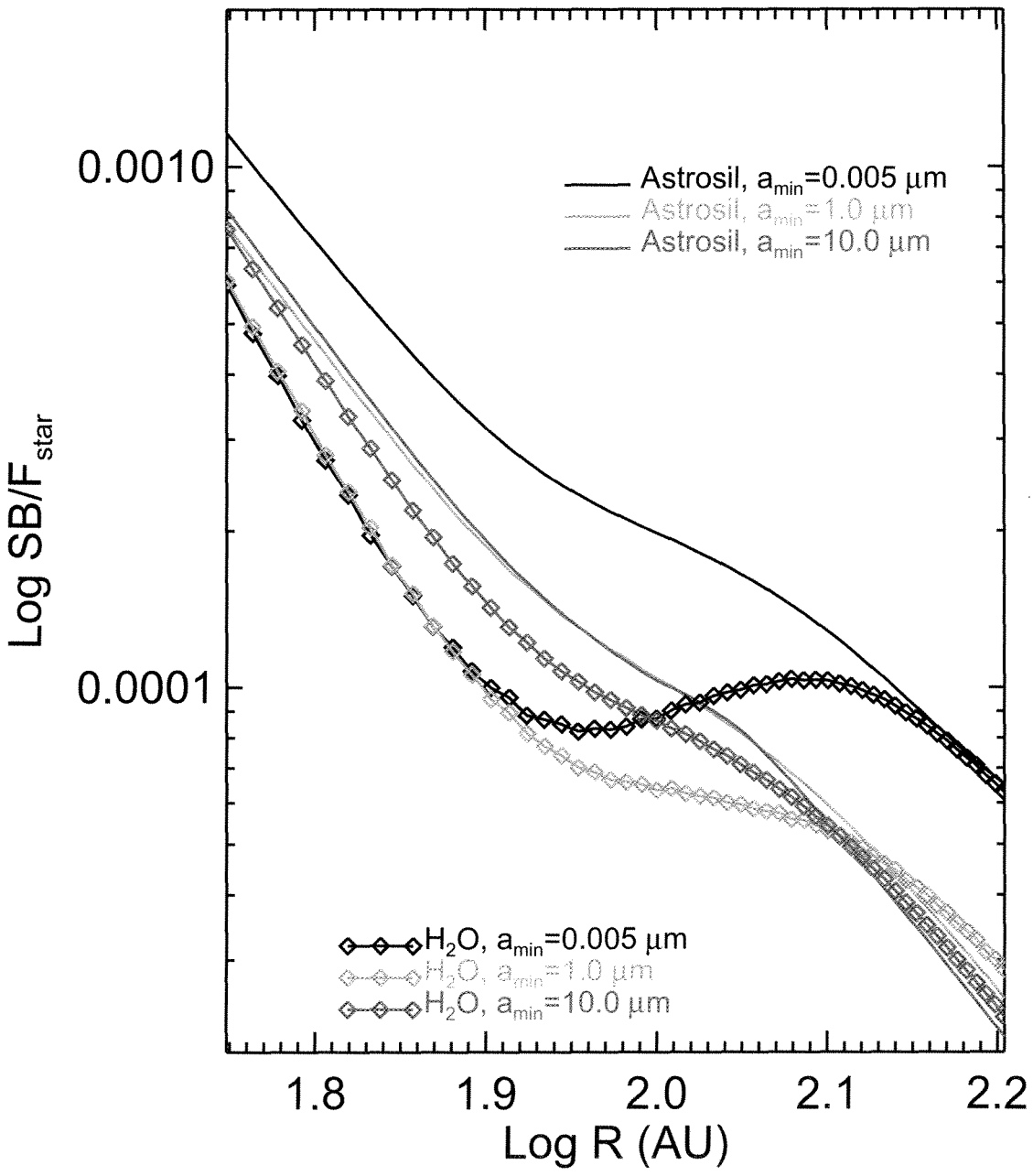

Fig. 7.— Comparison of TW Hya-like disk surface brightness profiles for different pure water ice (squares) and pure astronomical silicate (solid and dashed lines) compositions at the STIS bandpass.

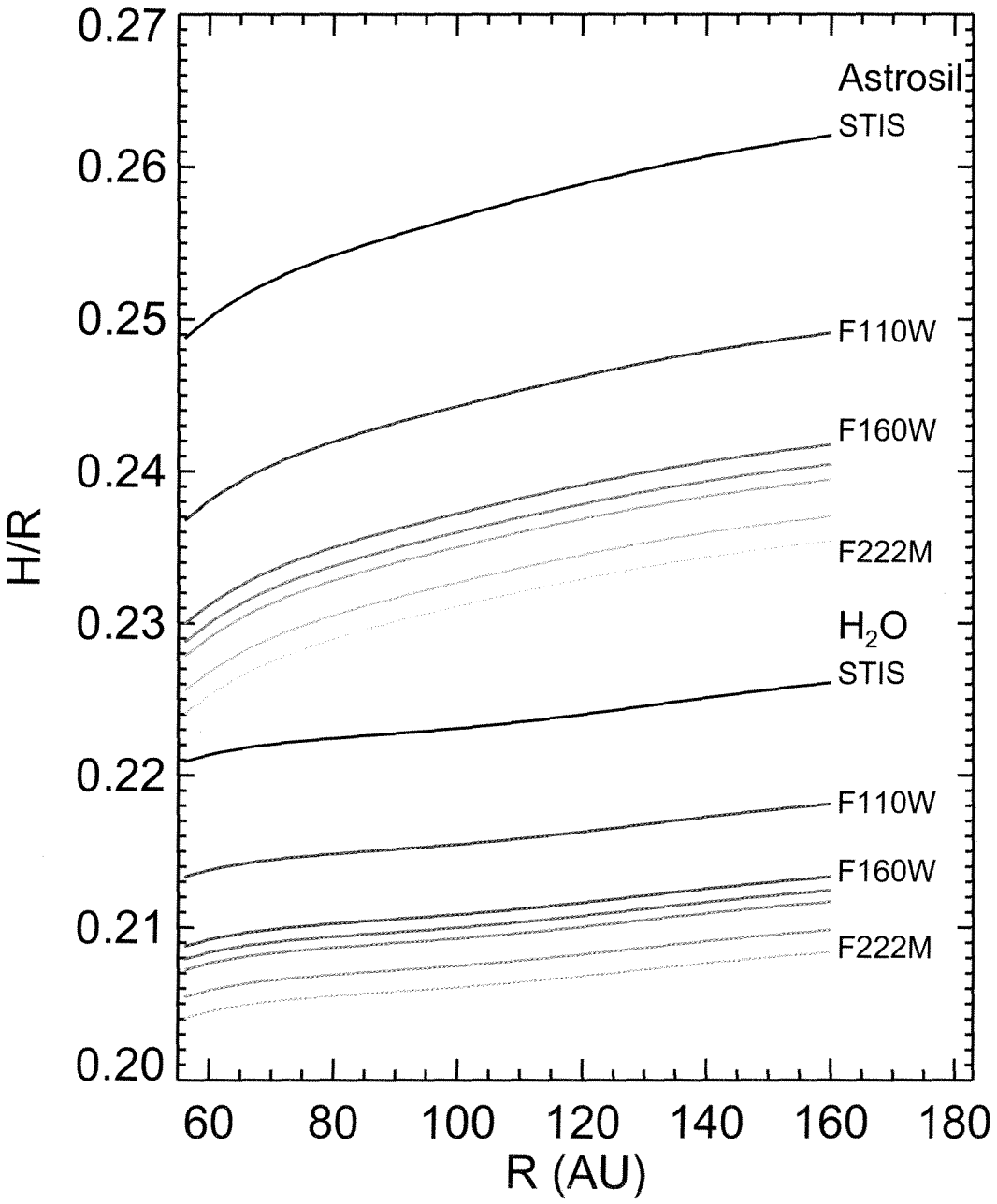

Fig. 8.— A comparison of H/R for astronomical silicates (blue lines) and water ice (red lines) with a_{min}=0.005μm, where H is the $\tau = 2/3$ optical depth surface at each wavelength. As expected, longer wavelength filters probe deeper within the disk surface, though the specific geometry of that surface changes with composition.

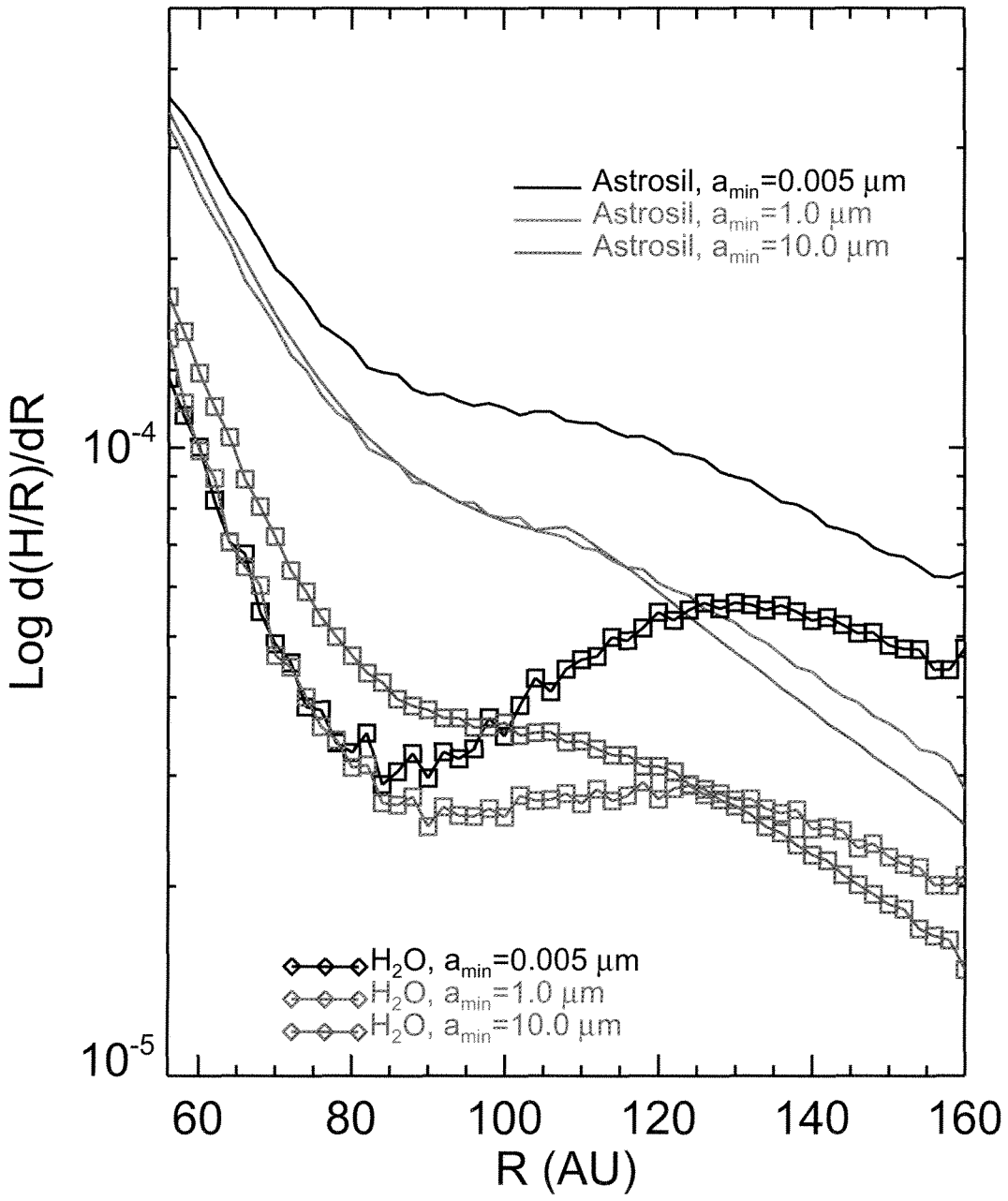

Fig. 9.— Comparison of d(H/R)/dR for pure water ice and astronomical silicate compositions of differing a_{min}. The derivative of the disk surface goes into the calculation of scattered light as discussed in §4.3.

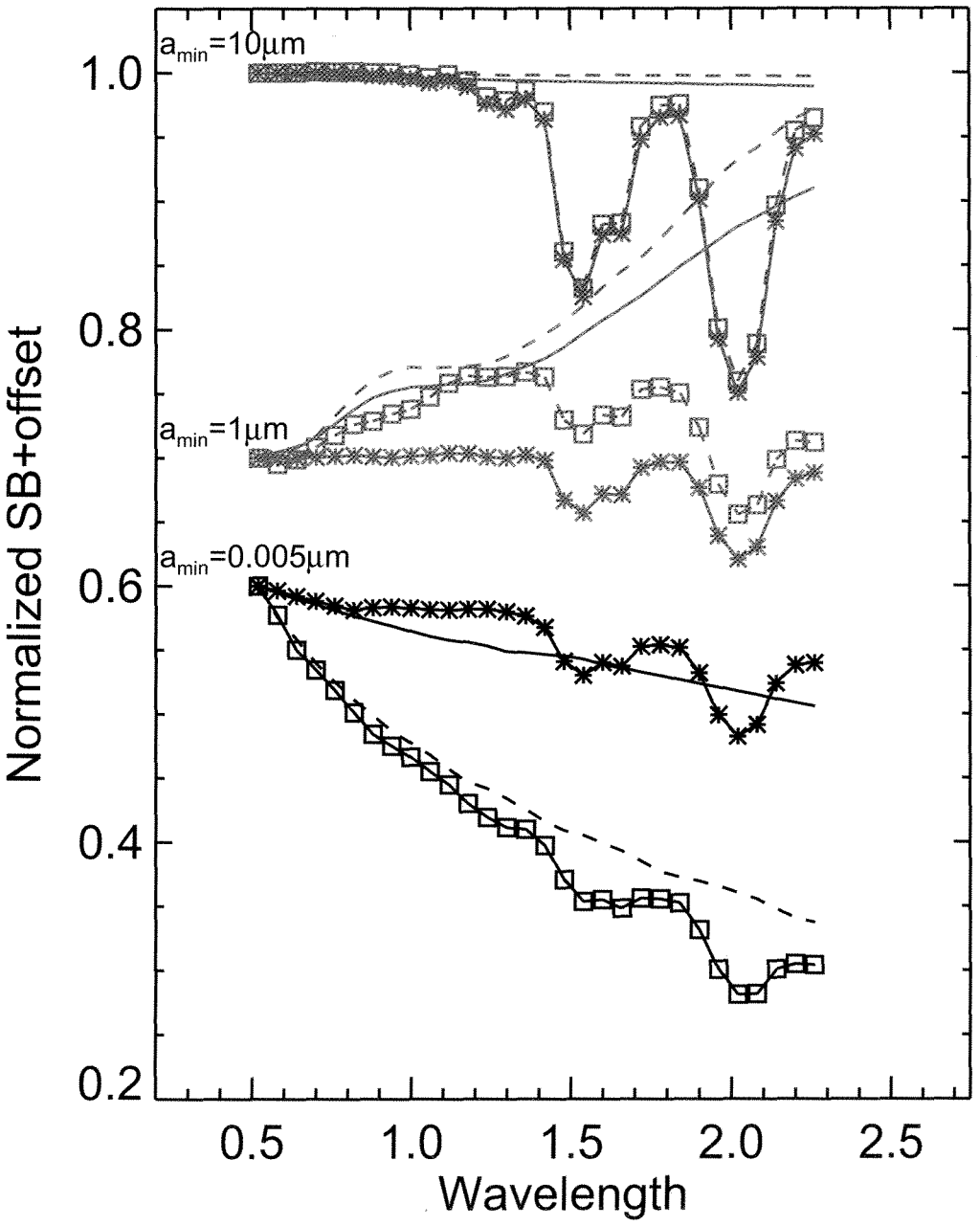

Fig. 10.— Comparison of TW Hya-like disk reflectance spectra for different pure water ice (squares and asterisks) and pure astronomical silicates (solid and dashed lines). Squares and solid lines represent the interior of the disk at 56 AU, while asterisks and dashed lines represent the outer part of the disk at 140 AU,

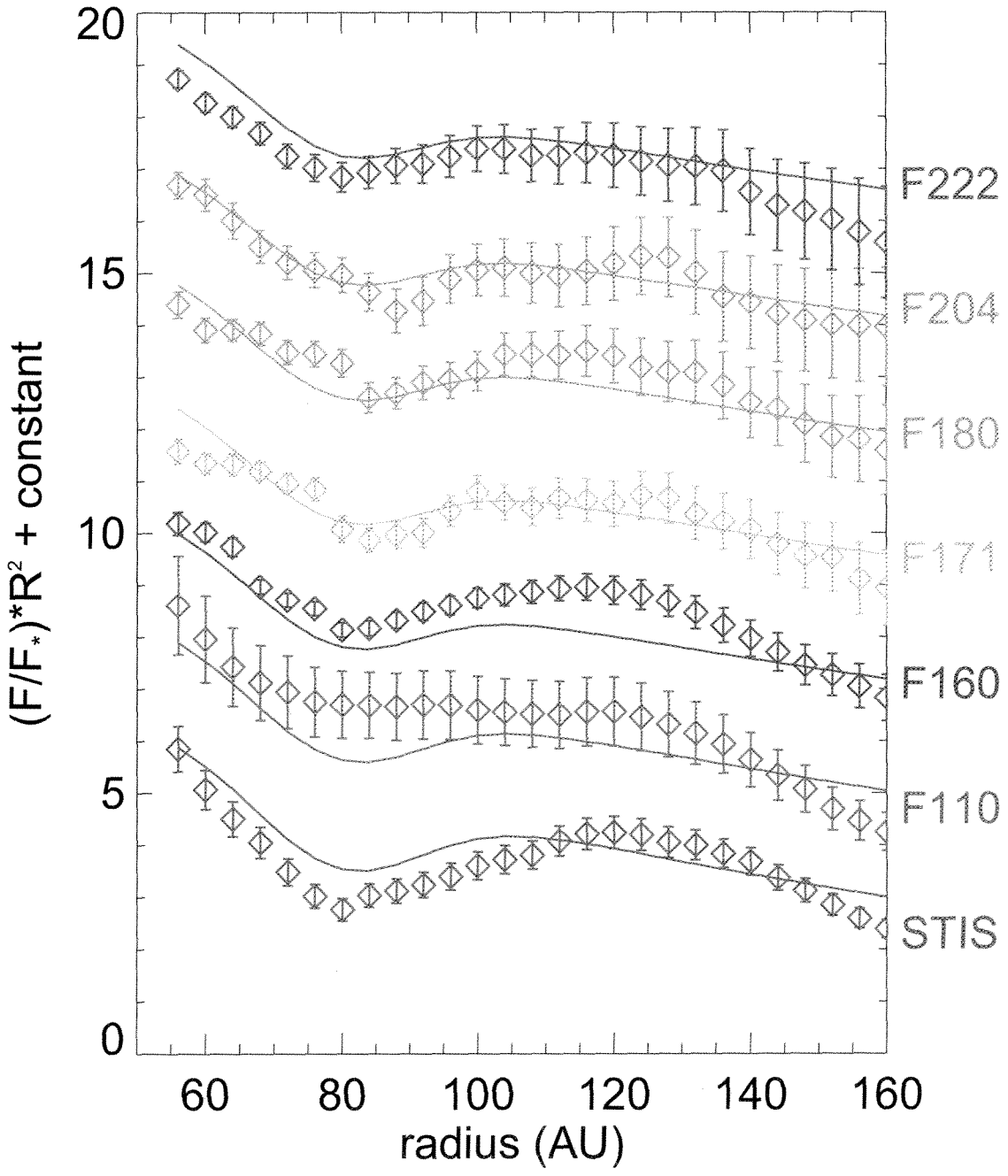

Fig. 11.— Comparison of radial profiles of the disk with model profiles from the best fitting disk model of §4.4.

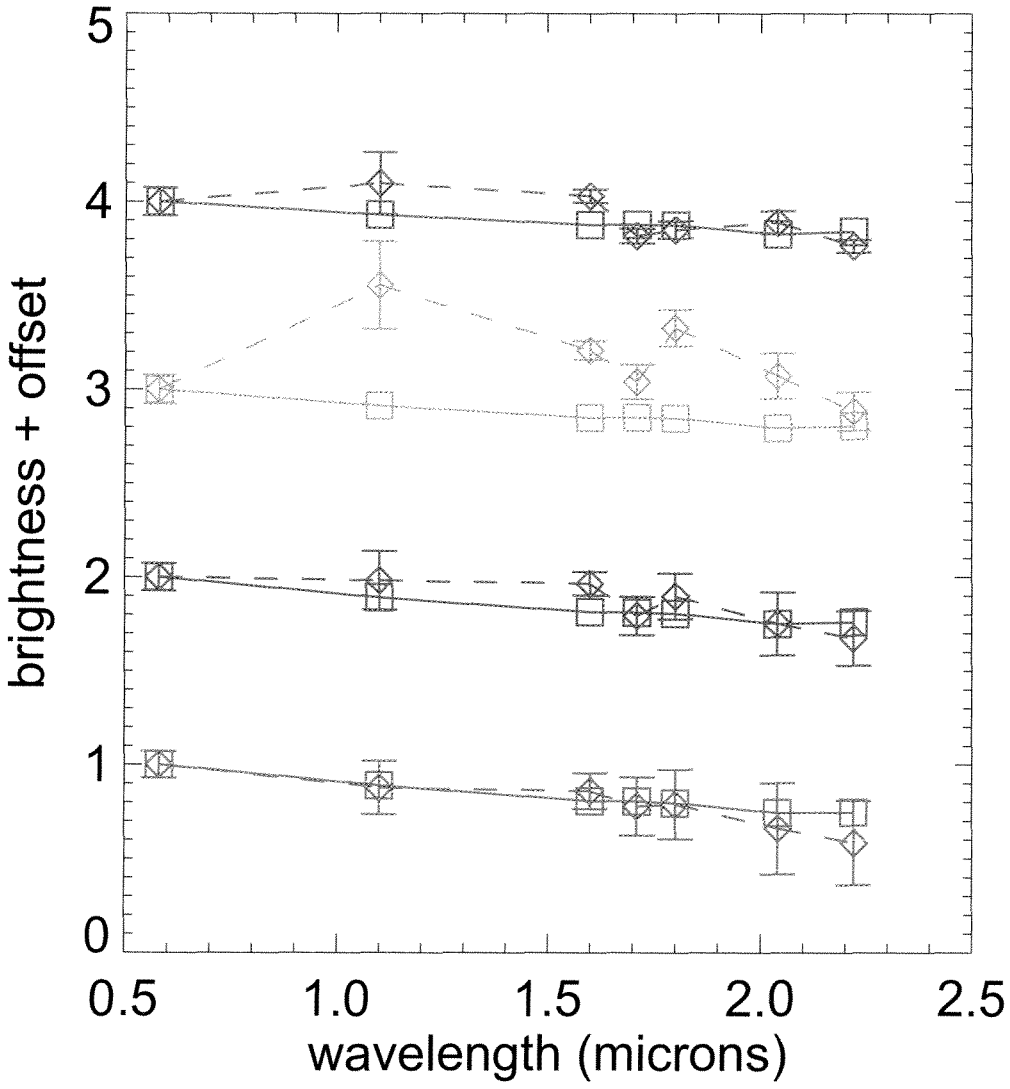

Fig. 12.— Comparison of radial spectra of the disk with model profiles from the best fitting disk model of §4.4. The spectra are normalized to the brightness at the STIS wavelength of 0.58 μm and offset vertically by whole numbers, starting with 3 for 60 AU, 2 for 80 AU, 1 for 120 AU, and 0 for 140 AU.

Table 1. Photometry of TW Hya and PSF Scalings

Filter	PSF Reference Star	Scaling	TW Hya Flux Density (Jy)
STIS 50CCD	HD 85512	0.0544,0.0586	0.1955
F110W	τ^1 Eridani	0.099±0.0027	0.747
F160W	Gl 879	0.031±0.002	1.03
F171M	CD-43°2742	0.541±0.008	0.94±0.01
F180M	CD-43°2742	0.528±0.001	0.84±0.01
F204M	CD-43°2742	0.56±0.01	0.77±0.01
F222M	CD-43°2742	0.61±0.01	0.76±0.02